

# Quantifying Photothermal and Hot Charge Carrier Effects in Plasmon-Driven Nanoparticle Syntheses

*Rifat Kamarudheen*<sup>†, ‡</sup>, *Gabriel W. Castellanos*<sup>†</sup>, *Leon P. J. Kamp*<sup>§</sup>, *Herman J. H. Clercx*<sup>§</sup>,

*Andrea Baldi*<sup>\*†, ‡</sup>

<sup>†</sup>DIFFER - Dutch Institute for Fundamental Energy Research, De Zaale 20, 5612 AJ Eindhoven,  
The Netherlands

<sup>‡</sup>Institute for Complex Molecular Systems, Eindhoven University of Technology, P.O. Box 513,  
5600 MB Eindhoven, The Netherlands

<sup>§</sup>Fluid Dynamics Laboratory, Department of Applied Physics, Eindhoven University of  
Technology, 5600 MB Eindhoven, The Netherlands

Corresponding author email address: [a.baldi@differr.nl](mailto:a.baldi@differr.nl)

**KEYWORDS:** plasmonics, nanoparticle synthesis, core@shell, photothermal synthesis, hot charge carriers

**ABSTRACT:** The excitation of localized surface plasmon resonances in Au and Ag colloids can be used to drive the synthesis of complex nanostructures, such as anisotropic prisms, bipyramids, and core@shell nanoparticles. Yet, after two decades of research, it is challenging to paint a complete picture of the mechanisms driving such light-induced chemical transformations. In

particular, while the injection of hot charge carriers from the metal nanoparticles is usually proposed as the dominant mechanism, the contribution of plasmon-induced heating can often not be neglected. Here, we tackle this uncertainty and quantify the contribution of different activation mechanisms using a temperature-sensitive synthesis of Au@Ag core@shell nanoparticles. We compare the rate of Ag shell growth in the dark at different temperatures with the one under plasmon excitation with varying laser intensities. Our controlled illumination geometry, coupled to numerical modeling of light propagation and heat diffusion in the reaction volume, allows us to quantify both localized and collective heating effects and determine their contribution to the total growth rate of the nanoparticles. We find that non-thermal effects can be dominant and their relative contribution depends on the fraction of nanoparticle suspension under irradiation. Understanding the mechanism of plasmon-activated chemistry at the surface of metal nanoparticles is of paramount importance for a wide range of applications, from the rational design of novel light-assisted nanoparticle syntheses, to the development of plasmonic nanostructures for catalytic and therapeutic purposes.

In the past two decades, a lot of interest has been devoted to the development of light-assisted syntheses of hierarchical and anisotropic metal nanoparticles (NPs).<sup>1-3</sup> Such syntheses are driven by the excitation of localized surface plasmon resonances (LSPRs) in noble metal nanoparticles and can result in nanostructures with high yields and narrow size and shape distributions.<sup>4-6</sup> The decay of LSPRs *via* non-radiative heat dissipation and the ejection of hot charge carriers are primarily responsible for these plasmon-assisted syntheses.<sup>5,7</sup>

One of the milestones in the field of plasmon-assisted nanoparticle synthesis is the photochemical transformation of spherical Au and Ag seeds into triangular prisms. These reactions are thought to proceed *via* the plasmon-mediated excitation of short-lived (< 100 fs)<sup>8</sup>

hot charge carriers and their subsequent injection into adsorbed organic ligands on the metal nanoparticle surface. In the case of silver sphere to prism transformation, the citrate molecules present on the silver seeds are photo-oxidized by the injection of hot holes, thereby generating a negative photovoltage on the seed particles and facilitating the reduction of  $\text{Ag}^+$  ions.<sup>3,5,9</sup> In the case of Au sphere to prism transformation, it has been shown that the surface ligand polyvinylpyrrolidone (PVP) increases the lifetime of plasmonically produced hot electrons *via* interfacial coulombic interactions. These electrons are then injected into adsorbed  $\text{Au}^{3+}$  ions at the surface of the gold seeds.<sup>2</sup> Such hot charge carrier driven mechanisms are further supported by photo-electrochemical measurements of nanoparticle-decorated electrodes,<sup>10-12</sup> as well as by the characterization of the redox states of the involved organic ligands and the wavelength and polarization dependence of the reaction kinetics.<sup>3,10</sup>

Despite these significant insights into the mechanism of plasmon-driven nanoparticle synthesis, several open questions remain on the efficiency of hot charge carrier driven reactivity and on the role and magnitude of light-induced heating.<sup>13,14</sup> Due to the strong light and temperature sensitivity of these nanoparticle syntheses, disentangling the relative contributions of hot charge carrier and photothermal effects is experimentally challenging. Furthermore, despite recent developments,<sup>15-20</sup> a theoretical understanding of the mechanism and efficiency of hot electron generation in metal nanoparticles and of their injection in molecular adsorbates under actual reaction conditions is still at its infancy.

Under continuous wave (CW) irradiation, the non-radiative decay of LSPRs leads to a local increase of the nanoparticle surface temperature with respect to its surrounding medium,  $\delta T$ , which is proportional to the particle absorption cross-section  $\sigma_{abs}$  and inversely proportional to its diameter  $d$  according to:<sup>21</sup>

$$\delta T = \frac{Q}{2\pi\kappa d} = \frac{\sigma_{abs} I}{2\pi\kappa d} \quad (1)$$

where  $Q$  is the absorbed power,  $I$  is the optical power per unit area and  $\kappa$  is the thermal conductivity of the medium surrounding the nanoparticle. In most light-driven syntheses reported in the literature, the low optical power used leads to a predicted local temperature increase at the surface of the metal nanoparticles of the order of milliKelvins.<sup>5</sup> As a consequence, localized plasmonic heating has generally been ruled out as an activation mechanism for these transformations. However, depending on the number density of the nanoparticles, even a slight increase of a few milliKelvins in  $\delta T$  on the nanoparticle surface can result in an increase of up to tens of Kelvins of the solution temperature, due to collective heating effects.<sup>22</sup> For example, collective plasmonic heating has been previously used to generate steam from water kept at room temperature,<sup>23</sup> for fractional distillation of azeotropic mixtures,<sup>24</sup> and in photo-thermo-electric devices.<sup>25</sup> Such macroscopic temperature increases could easily be sufficient to activate endothermic reactions, such as the citrate mediated reduction of silver ions used in Ag nanoparticle transformations.<sup>5</sup> Furthermore, it has been proposed that the surface redox potentials of metal nanoparticles and the rate of charge transfer at their surface can be significantly influenced by temperature.<sup>7</sup> As such, quantifying the contributions of localized and collective plasmonic heating is crucial for properly understanding the activation mechanism of light-driven nanoparticle syntheses.<sup>26</sup>

In the limit of low light scattering and no convection, empirical equations have been derived to correlate the local temperature increase  $\delta T$ , to the collective increase in temperature of the irradiated volume of solution.<sup>22</sup> These equations, however, cannot be used when both scattering and absorption by the plasmonic nanoparticles strongly affect light propagation and large temperature gradients can develop across the liquid.<sup>27</sup> Under these conditions, mapping the three-

dimensional temperature distribution or estimating average temperatures inside reaction vessels during plasmon excitation is challenging. In light-driven syntheses, thermocouples are typically limited by the sensitivity of the thermoelectric probes to the incoming light. Furthermore, infrared (IR) cameras are restricted to measuring the surface temperatures of the chemical glassware, due to the low penetration depth of infrared radiation through glass or quartz. Alternative techniques such as Temperature Imaging using Quadriwave Shearing Interferometry (TIQSI) and Raman spectroscopy are limited to mapping temperature distributions over 2D surfaces.<sup>28,29</sup> For this reason, numerical modelling of light absorption and scattering as well as of heat transfer by conduction and convection are essential to derive a realistic picture of the temperature distribution in reaction vessels for light-activated chemistry.<sup>27</sup>

Here, we quantitatively assess the effect of local and collective plasmon-induced heating in a plasmon-driven nanoparticle synthesis, using a combination of experimental and numerical methods. First, we develop a temperature-sensitive synthesis of Au@Ag core@shell nanoparticles, in which the growth rate of the silver shell increases exponentially with the temperature of the solution. The formation of a silver shell on the gold nanoparticles leads to a marked increase in their extinction cross-section, which we follow spectroscopically during the reaction. Second, we study the rate of Ag shell growth under plasmon excitation using monochromatic light with varying optical power, in the absence of any external heating. Third, we use numerical modelling to simulate light propagation and heat transfer by conduction and convection to quantify temperature distributions in our reaction vessel under experimental conditions. Finally, by comparing the observed shell growth rates under light irradiation to the ones measured in the dark, and in light of the numerical results, we quantify the relative contributions of photothermal and hot charge carrier effects to the total growth rate of the Ag

shell. In our experimental conditions the effect of localized heating is negligible, leading to surface temperature increases of the order of a few milliKelvins. Collective heating effects, however, can account for 30% to nearly 100% of the total reaction rate, depending on the volume fraction of nanoparticle solution under illumination. The remaining observed activity is attributed to electromagnetic effects, such as the hot electron driven reduction of  $\text{Ag}^+$  ions at the surface of Au nanoparticles.

## RESULTS AND DISCUSSION

### **Ag shell growth in the dark.**

Large spherical Au nanoparticles with a diameter of  $69 \pm 11$  nm (measured over 1765 particles) were synthesized adapting a previously reported method (Figure 1A).<sup>30</sup> This nanoparticle size has been chosen to maximize the increase in surface temperature for Au nanospheres capped with the surfactant cetyltrimethylammonium chloride (CTAC) under a 532 nm laser irradiation. Smaller particles have lower absorption cross-sections thereby generating lower temperature increases. Larger particles, despite having a larger absorption cross-section at 532 nm, distribute the absorbed power over larger volumes, leading to lower overall temperature increases (see Supporting Information, SI 1).

In order to assess the effects of plasmonic heating, we designed a temperature-activated synthesis of Au@Ag core@shell nanoparticles (see Figure 1B and the Materials and methods section). Our final objective is to properly quantify different contributions to the total reaction rate during laser (532 nm) irradiation experiments. For this reason, we want to minimize the variation in the absorption cross-section of Au@Ag nanoparticles during the shell growth reaction (see eq (1)). We, therefore, limit our reactions to the growth of very thin (0-3 nm) Ag

shells (see SI 2). Briefly, aqueous solutions containing  $\text{AgNO}_3$ , bis(p-sulfonatophenyl)phenylphosphine (BSPP), and ascorbic acid are added sequentially to CTAC stabilized Au nanoparticle suspensions. The water-soluble ligand BSPP is used to complex free  $\text{Ag}^+$  ions and control the shell growth rate.<sup>9,31</sup> In our studies, we follow the silver shell growth by measuring the variation in the extinction spectra of our Au@Ag nanoparticle suspensions. We optimize the relative molar concentrations of BSPP and  $\text{Ag}^+$  between 1 and 3.3, and we find that for a ratio of  $[\text{BSPP}]/[\text{Ag}^+] = 2.5$ ,  $\text{Ag}^+$  reduction is kinetically inhibited at room temperature. At 60 °C, however, such a ratio leads to the growth of a silver shell on the Au nanoparticles as evidenced by a large increase in their extinction spectra in the  $\lambda < 500$  nm range (Figure 1C). The observed change in extinction is consistent with an Ag shell growth rate of  $\sim 1.5$  nm in thickness per hour, as evidenced by Mie theory calculations of the extinction spectra of Au@Ag nanoparticles (Figure 1D).

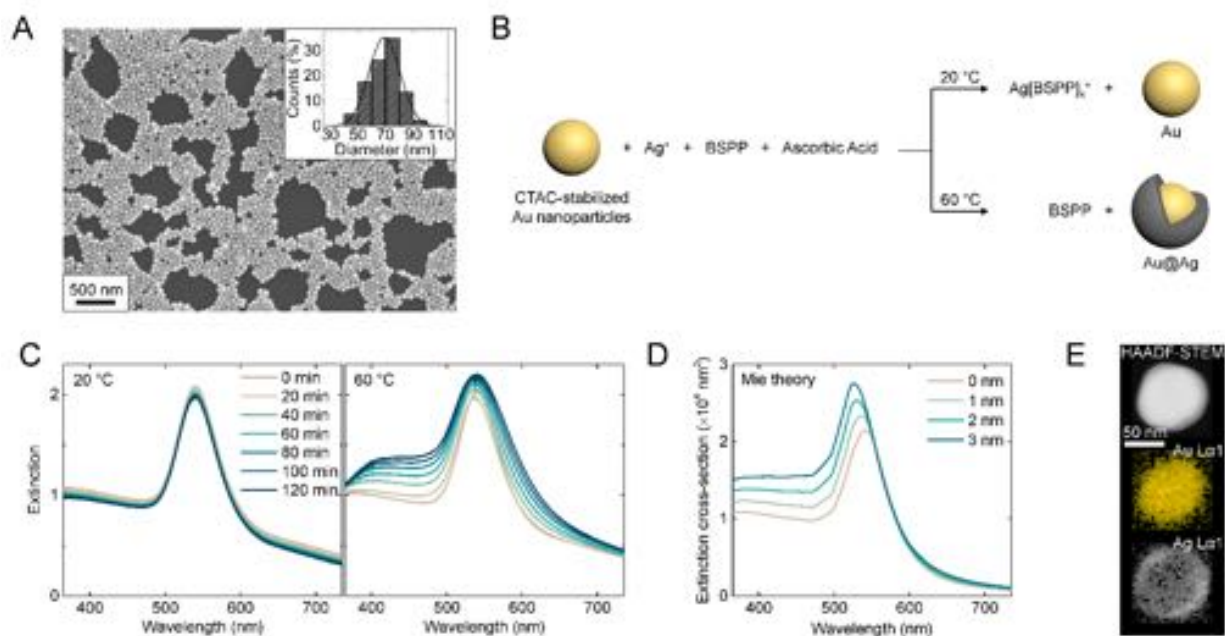


**Figure 1.** (A) Representative SEM image of Au nanoparticles before Ag shell growth. The inset shows the measured size distribution. (B) Schematic representation of the temperature-activated

synthesis of Au@Ag core@shell nanoparticles in the dark. (C) Time evolution of the extinction spectra of the reaction mixture in the dark (left) at 20 °C and (right) at 60 °C. (D) Extinction cross-section of Au@Ag core@shell nanoparticles with 69 nm Au diameter and varying Ag shell thicknesses, calculated using Mie theory with literature dielectric data for Au and Ag.<sup>32</sup> (E) High-Angle Annular Dark-Field Scanning Transmission Electron Micrograph (HAADF-STEM) and corresponding Energy Dispersive X-ray (EDX) maps of Au L $\alpha$ 1 and Ag L $\alpha$ 1 signals for an Au@Ag core@shell nanoparticle grown in the dark at 60 °C for 6 hours.

The growth of an Ag shell is further confirmed by elemental mapping using energy dispersive X-ray spectroscopy (EDX), as shown in Figure 1E. The formation of Ag shells on Au nanoparticles at moderately high temperatures suggests the dissociation of Ag[BSPP]<sub>x</sub><sup>+</sup> complexes to release free Ag<sup>+</sup> ions, which are subsequently reduced by ascorbic acid, to form Au@Ag core@shell nanoparticles. Such temperature-driven dissociation of silver-phosphine complexes have already been observed in organic solvents.<sup>33</sup>

In order to quantify the growth rate of the Ag shell, we monitor the temporal evolution of the extinction spectra of Au@Ag nanoparticles in the wavelength range between 397 nm and 477 nm. In this spectral region, the features due to Ag are most prominent and minimally affected by the dipole resonances of the core@shell nanoparticles (see SI 3). We define an extinction contrast parameter, *EC*, that accounts for the relative increase in extinction at time *t* with respect to the extinction at time *t* = 0:

$$EC = \frac{\int_{397 \text{ nm}}^{477 \text{ nm}} Ext(t) d\lambda - \int_{397 \text{ nm}}^{477 \text{ nm}} Ext(0) d\lambda}{\int_{397 \text{ nm}}^{477 \text{ nm}} Ext(0) d\lambda}$$

In Figure 2A, we plot the time evolution of the extinction contrast for a silver shell growth reaction in the dark at 60 °C. Similar trends are observed for all reaction temperatures, with

higher temperatures leading to faster shell growth (see SI 4). The reaction proceeds through three different regimes: i) an *induction* period during which the solution temperature equilibrates to the final value and the *EC* initially decreases and then recovers, ii) a *growth* period (orange dots) in which the *EC* increases linearly with time due to the silver shell formation, and iii) a *depletion* period during which the shell growth slows down due to the decreasing concentration of free  $\text{Ag}^+$  ions in solution.

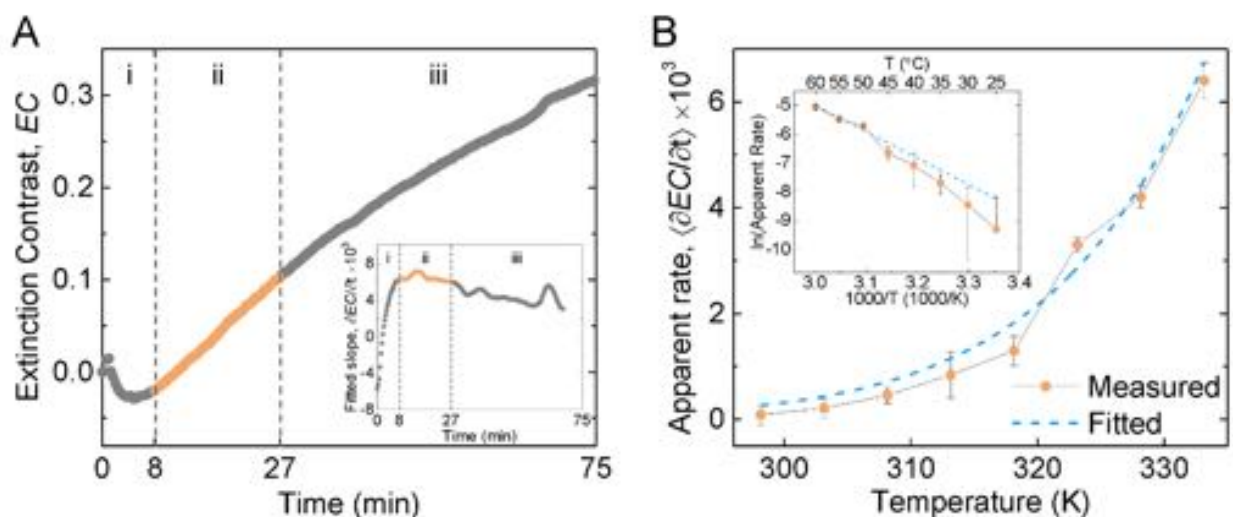


**Figure 2.** (A) Time evolution of the extinction contrast,  $EC$ , during the Ag shell growth reaction at 60 °C in the dark. The inset shows the time evolution of the slope  $\partial(EC)/\partial t$ . (B) Apparent rate of the Ag shell growth reaction in the dark as a function of temperature. The dashed line is a fit to the data using eq (2). The inset shows the same data as an Arrhenius plot.

The inset in Figure 2A shows the time evolution of the fitted slope for the “ $EC$  vs Time” plot, calculated by fitting a straight line through 20 data points between  $t_n$  and  $t_{n+19}$ : (i) in the induction period the slope increases from negative to positive values, (ii) during the growth regime the slope  $\partial(EC)/\partial t$  is roughly constant and the mean and standard deviation of the slope in this regime are used to define an *apparent rate* of the reaction,  $\langle\partial(EC)/\partial t\rangle$ , (iii) in the depletion regime the slope slowly decreases. The decrease in the extinction intensity during the induction

period is most likely due to the change in the packing density of the CTAC bilayer around the Au nanoparticle surface (SI 5). Interestingly, the higher the reaction temperature, the faster the shell growth begins, and the shorter is the induction period (SI 4).

During the growth period, the extinction contrast increases linearly with time, indicating that the concentration of  $\text{Ag}^+$  ions in solution is roughly constant. For small Ag shell thicknesses (0 - 3 nm), the extinction contrast scales linearly with the number of reduced silver atoms, and we can therefore write the following rate equation (see details in SI 6):

$$\frac{\partial(EC)}{\partial t} \approx \text{constant} \cdot \exp\left(-\frac{E_a}{RT}\right) \quad (2)$$

In Figure 2B, we plot the apparent rate,  $\langle \partial(EC)/\partial t \rangle$ , as a function of the nanoparticle solution temperature  $T$ . An exponential fit to the data using eq (2) leads to an activation energy for the silver shell growth of  $76 \pm 10$  kJ/mol, which is comparable to the one measured for other temperature-activated Ag nanoparticle syntheses.<sup>34</sup>

### **Ag shell growth under plasmon excitation.**

After having characterized the temperature dependence of the silver shell growth rates in the dark, we repeated the synthesis by irradiating the growth solution at the Au plasmon resonance in the absence of any external heating. We perform this experiment on a 90  $\mu\text{L}$  nanoparticle growth solution placed in a 10 mm  $\times$  2 mm quartz cuvette, inside a home-built setup that allows simultaneous laser irradiation and extinction spectroscopy (see SI 7 and the Materials and methods section). We excite the plasmon resonance of the Au nanoparticles using a 532 nm CW laser of varying optical powers ranging from 100 mW to 440 mW. For sufficiently high laser intensities, we observe an extinction increase similar to the one observed for the nanoparticle solutions heated in the dark, indicating the formation of a silver shell on the Au nanoparticles

(Figure 3A). As shown in Figure 3B, higher laser intensities lead to faster rates of silver shell growth.

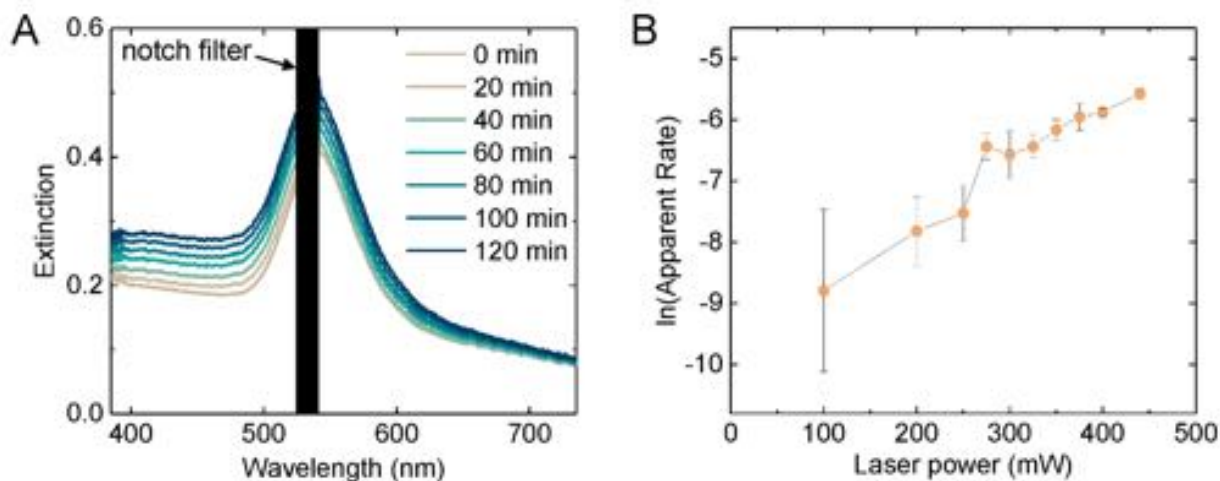


**Figure 3.** (A) Time evolution of the extinction spectra of Au nanoparticles suspended in Ag shell growth solution, under a 532 nm laser irradiation at an optical power of 400 mW, corresponding to an intensity of  $\sim 23 \text{ W/cm}^2$  (Gaussian profile, beam width  $1/e^2 = 1.5 \text{ mm}$ ). (B) Natural logarithm of the apparent rate of silver shell growth as a function of the laser irradiation power.

In order to understand the Ag shell growth reaction dynamics under plasmon excitation, we can compare the apparent rates observed under laser irradiation (Figure 3B) with the Arrhenius plot obtained from the temperature-activated syntheses in the dark (inset in Figure 2B). For example, the rate measured for a laser power of 400 mW is comparable to the one observed when the nanoparticle solution is heated to a temperature of  $\sim 50 \text{ }^\circ\text{C}$  in the dark. To determine if the observed activity under plasmon excitation is purely due to a photothermal process, it is necessary to evaluate the steady-state temperature profile in our solution during laser irradiation. The use of thermocouples is hindered by their limited spatial resolution compared to our reaction volume ( $90 \text{ } \mu\text{L}$ ) and by their typical high sensitivity to light, which prevents us from measuring temperatures inside the illumination path (SI 8).<sup>22</sup> Temperature measurements using IR cameras,

on the other hand, are limited to measuring surface temperatures of our reaction vessels, due to the low IR transmittance of our quartz cuvettes.<sup>35</sup> Interestingly, upon irradiation of a suspension of Au NPs with 400 mW laser power for 30 min the surface temperature of the cuvette only increases by  $\sim 8$  °C (SI 9). To properly evaluate temperature profiles inside our nanoparticle suspension during plasmon-induced reactions, we therefore use numerical methods to model light propagation and heat transfer by conduction and convection in our system.

### **Light propagation and heat transfer.**

The propagation of light in a scattering and absorbing medium is described by the radiative transfer equation (RTE).<sup>36</sup> Our experiments are performed on suspensions of Au nanoparticles of 69 nm in diameter with a nanoparticle density of  $2.24 \times 10^{10}$  NPs/mL, corresponding to an optical density of 1.92 at 532 nm for an optical path length of 1 cm. Such nanoparticle suspensions are highly scattering and highly absorbing at the wavelength used for laser irradiation. For this reason, we cannot use approximate solutions to the RTE that are valid for light propagation in a non-scattering (Beer-Lambert equation) or non-absorbing (diffusion equation) media.<sup>37</sup> To properly account for light scattering and absorption in our reaction volume, we developed a Monte Carlo model that simulates photon propagation in a suspension of metal nanoparticles.<sup>38</sup> Our model uses realistic probabilities of photon scattering and absorption, from cross-sections calculated with Mie theory,<sup>39</sup> and considers an exponential probability density distribution in photon scattering path length, in agreement with what is expected from light propagation in a medium with random scatterers.<sup>40</sup> To calculate the angular distribution of the scattered photons, we approximate the radiation profile of our 69 nm Au nanoparticles with the one of a perfect electric dipole (SI 10). The 90  $\mu$ L nanoparticle solution, which is contained in a  $2 \times 10 \times 4.5$  mm<sup>3</sup>

volume, is divided into cubic unit cells of 0.1 mm edge length. In our Monte Carlo calculations, we inject photons into the simulation volume, with a spatial distribution and a propagation direction matching our experimental laser beam profile. At each iteration of the model, the photon travels a distance corresponding to a calculated path length and it is then either absorbed or scattered. If the photon is scattered, a new propagation direction is generated from the scattering profile and the process is repeated. If the photon is absorbed, the event is registered into a matrix  $N_{abs}(i_x, i_y, i_z)$ , where  $i_x$ ,  $i_y$ , and  $i_z$  are the indices corresponding to the unit cell in which the absorption process occurred. Our model also takes into account, the reflection and transmission of photons at the liquid/quartz (sides and bottom) and liquid/air (top) interfaces, using Fresnel's equations. From the Monte Carlo simulation, we find that only a fraction of photons are transmitted through the cuvette of  $\sim 1.5\%$ , corresponding to an optical density of 1.8, which is in good agreement with the measured value. Given an incident optical power,  $P_{inc}$ , and a total number of simulated photons,  $N$ , we can calculate the optical power absorbed in each unit cell of volume  $dV$  as:<sup>27</sup>

$$q(i_x, i_y, i_z) = \frac{N_{abs}(i_x, i_y, i_z)P_{inc}}{N dV} \quad (5)$$

We find that under our experimental conditions (532 nm laser beam with optical power of 400 mW and a  $1/e^2$  beam width of 1.5 mm) most of the photons are absorbed in the first few millimetres of the nanoparticle suspension (Figure 4A). From the absorbed power and the nanoparticle density, we can then calculate the local increase in the surface temperature of the Au nanoparticles,  $\delta T$ , using eq (1). The use of eq (1) is justified, as it has been shown that temperature deviations due to a finite interface conductivity are negligible for Au nanoparticles capped with cetyltrimethylammonium salts.<sup>41</sup> Interestingly, even at an irradiation power of 400 mW, the maximum local temperature increase is a negligible 8 mK (Figure 4A), with an average

surface temperature increase in the solution of  $\sim 0.6$  mK. These values are much too small to justify any Ag shell growth due to a local increase in the surface temperature of the Au nanoparticles. However, at high enough nanoparticle densities, collective heating effects can arise, leading to a macroscopic temperature increase of the solution.<sup>22</sup> Due to the highly inhomogeneous distribution of the absorbed power and the complex heat transfer mechanism in our reaction cuvette, composed of both conduction and convection processes, it is not possible to derive an analytical equation to calculate the average solution temperature.

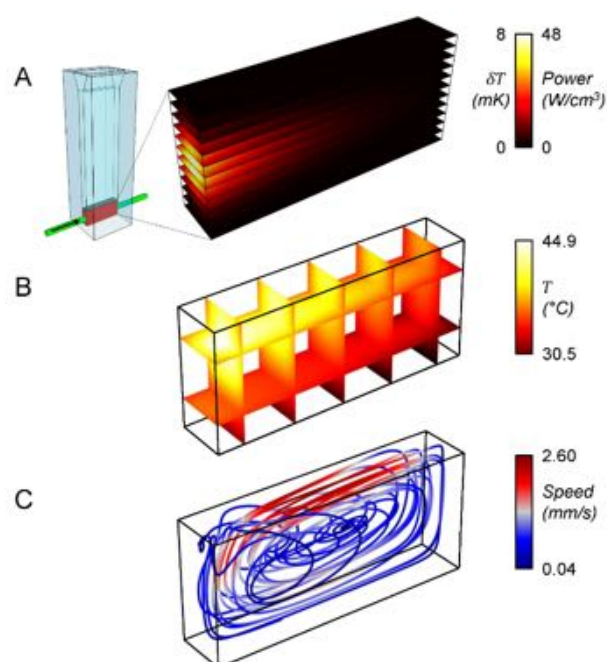


**Figure 4.** (A, left) Schematic illustration of the irradiation geometry for a 90  $\mu\text{L}$  volume of nanoparticle suspension inside our quartz cuvette. The zoomed-in image shows the 3D spatial distribution of the absorbed optical power per unit cell,  $q(i_x, i_y, i_z)$ , and of the local temperature increase,  $\delta T$ . (B) Steady-state temperature profile inside the nanoparticle solution due to collective heating effects, after 30 min of laser irradiation, calculated using COMSOL. (C)

Convection induced fluid flow for an irradiated nanoparticle solution visualized by Lagrangian fluid parcel trajectories using COMSOL.

We, therefore, employ a Finite Element Method (FEM, COMSOL) to compute the magnitude and spatial profile of the solution temperature inside our cuvette, using the heat power density derived from the Monte Carlo simulations as heat source input. Figure 4B shows the computed steady-state temperature distribution inside the reaction volume after 30 minutes of laser irradiation. Notably, a large temperature gradient of the order of  $\sim 1$  °C/mm is present in the liquid. Such a spatial inhomogeneity would lead to significant errors when estimating the average solution temperature using a single thermocouple measurement. Furthermore, we find that laminar flow convection is the dominant mechanism of heat exchange over conductive heat transfer in the nanoparticle solution, with fluid velocities as large as 2.6 mm/s (Figure 4C). Similar high velocities have been measured in plasmonically-heated solutions using scattering glass beads.<sup>22</sup> The COMSOL calculated magnitudes and rates of temperature increase at different locations in the solution and at the surface of the cuvette agree quantitatively with IR camera and thermocouple measurements performed during laser irradiation (SI 11). Most notably, we find that upon laser irradiation with 400 mW optical power, the average solution temperature calculated with COMSOL reaches a steady-state value of 37 °C in about 10 min (SI 12).

An average solution temperature of 37 °C is significantly lower than the 50 °C we estimated comparing the rates in Figures 2B and 3B. In particular, we find that in our light-driven synthesis at 400 mW, collective heating effects can only account for  $\sim 30\%$  of the total reaction rate. The remaining  $\sim 70\%$  must be due to non-thermal effects, such as hot electron driven reduction of  $\text{Ag}^+$  ions on the Au nanoparticle surface or two-photon mediated reduction of  $\text{Ag}^+$  to  $\text{Ag}^0$  assisted by the near-field enhancements on the Au nanoparticle surface. The latter process has been

previously demonstrated under 800 nm femtosecond laser pulsed irradiation and has been attributed to the higher reduction potential of photo-excited silver ions.<sup>42</sup> Two-photon mediated processes can also be carried out with CW lasers with very high power densities<sup>43</sup> (of the order of MW/cm<sup>2</sup>) or using optimized metallic substrates that can highly enhance the near-fields on the particle surface (>30,000x).<sup>44</sup> In our work, however, we use CW laser power densities of the order of tens of W/cm<sup>2</sup> and gold nanoparticles with maximum near-field enhancements of about 35x (SI 13). Furthermore, we performed a control experiment in which we irradiated a Ag<sup>+</sup> growth solution with a laser power of 440 mW in the absence of Au nanoparticles: after 15 hours of continuous illumination, we did not observe any spectroscopic evidence of Ag nanoparticle formation, indicating that the Ag<sup>+</sup> ions are not sensitive to our irradiation conditions (SI 14).

Given the above considerations, we can safely conclude that the principal mechanism of non-thermal activation in our reaction is the hot electron mediated reduction of silver ions and we can therefore estimate the efficiency of the hot electron-driven process. We define the hot electron internal quantum efficiency (IQE) as the number of Ag<sup>+</sup> ions reduced per photon absorbed by an Au nanoparticle. For a silver shell growth of ~2 nm, corresponding to a 400 mW irradiation over a period of 2 h, we find an average IQE over the reaction volume of ~10<sup>-6</sup>. Such low quantum yield is not necessarily surprising, considering that the size of our Au nanoparticles has been optimized to maximise photo-thermal effects and that smaller particles are expected to be more efficient sources of hot electrons.<sup>15,19</sup> Furthermore, our IQE implicitly includes efficiency losses due to the generation of hot charge carriers, their injection into chemical reactants, and any efficiency loss due to competing chemical reactions at the nanoparticle surface.

Interestingly, in light-driven syntheses we do not observe any induction period (SI 15), strongly suggesting that, under laser irradiation, the Ag shell growth starts immediately thanks to non-thermal activation processes.

Finally, it is important to note that the fraction of the irradiated volume of nanoparticle suspension also plays an important role in determining the relative contributions of photothermal and hot charge carrier effects in plasmon-driven reactions. When the volume of the nanoparticle suspension is increased from 90  $\mu\text{L}$  to 450  $\mu\text{L}$  under identical illumination conditions we find that, while the total reaction rate decreases, photothermal effects become the dominant contribution, essentially accounting for 100% of the total reaction rate (SI 16). This is a direct consequence of the fact that, while light propagation is only marginally affected by the volume increase, collective heating effects can extend to much longer distances, thanks to the large convection flows in the liquid.

## **CONCLUSIONS**

In summary, we have studied the mechanism of activation of a plasmon driven synthesis of Au@Ag core@shell nanoparticles. Our controlled reaction and illumination conditions, coupled to numerical modelling of light propagation and heat transfer processes by convection and conduction in the reaction volume, allow us to quantify the relative contributions of photothermal and electromagnetic effects. We find that hot charge carrier effects can be a dominant driving force in the silver shell growth reaction, but their relative contribution strongly depends on the irradiated volume fraction of nanoparticle suspension. Quantifying the non-radiative mechanisms contributing to plasmon-activated chemical reactions is essential for a wide range of applications. Our approach, combining experimental characterization and

numerical modelling, could therefore prove crucial to understand the plasmonic activation mechanisms of nanoparticle syntheses, drug delivery, and heterogeneous catalysis.

## METHODS

Gold(III) chloride trihydrate ( $\text{HAuCl}_4 \cdot 3\text{H}_2\text{O}$ ,  $\geq 99.9\%$  trace metals basis), Hexadecyltrimethylammonium bromide (CTAB,  $\geq 98\%$ ), Sodium borohydride ( $\text{NaBH}_4$ , 99%), Silver nitrate ( $\text{AgNO}_3$ , 99.9999% trace metals basis), L-Ascorbic acid ( $\geq 99\%$ ), Hexadecyltrimethylammonium chloride (CTAC,  $\geq 98.0\%$ ) and Bis(p-sulfonatophenyl)phenylphosphine dihydrate dipotassium salt (BSPP, 97%) were purchased from Sigma-Aldrich. All the solutions were prepared using deionized MilliQ water (18.2 M $\Omega$  at 25 °C).

*Synthesis of Au nanoparticles.* Au nanoparticles with an average diameter of 69 nm are synthesized adapting a previous report.<sup>30</sup> In order to obtain larger particles, the concentration of  $\text{HAuCl}_4$  and ascorbic acid are modified in steps (3) and (4). The seed-mediated synthesis is performed in four steps, as follows:

1) *Synthesis of ~1.5 nm spherical seeds:* In a typical synthesis, 125  $\mu\text{L}$  of 10 mM  $\text{HAuCl}_4$  solution is added into a CTAB solution (5 mL, 100 mM) under stirring, kept in a round bottom flask at 30 °C. Into the flask, an ice-cold  $\text{NaBH}_4$  solution (0.3 mL, 10 mM) is added. The solution is then kept stirring for 2 min and then left undisturbed for 1 h.

2) *Synthesis of gold nanorods:* In this step,  $\text{HAuCl}_4$  solution (2 mL, 10 mM),  $\text{AgNO}_3$  solution (240  $\mu\text{L}$ , 10 mM) and ascorbic acid solution (320  $\mu\text{L}$ , 100 mM) are added sequentially to a stirring CTAB solution (40 mL, 100 mM) at 30 °C. Afterwards, Au seeds (48  $\mu\text{L}$ ) from step (1) are added and the solution is stirred for 1 minute and then left undisturbed for 2 h. 40 mL of the above solution is centrifuged twice (20,000 xg, 10 min), the first time with redispersion in water (40 mL) and the second time in an aqueous CTAB solution (40 mL, 10 mM).

3) *Overgrowth of gold nanorods*: An aqueous H<sub>2</sub>AuCl<sub>4</sub> solution (20 mL, 10 mM) and an ascorbic acid solution (20 mL, 100 mM) are added sequentially to 40 mL of the centrifuged nanorod solution obtained from step (2), while stirring at 40 °C. The mixture is then left undisturbed overnight, maintaining the same temperature.

4) *Transformation into spherical nanoparticles*: 40 mL of the fattened gold nanorod solution from step (3) is centrifuged (20,000 xg, 10 min) and redispersed in an aqueous CTAB solution (40 mL, 10 mM). An H<sub>2</sub>AuCl<sub>4</sub> solution (8 mL, 10 mM) is then added and stirred for a minute. The mixture is then left undisturbed overnight, at 40 °C. The nanoparticles are centrifuged thrice (20,000 xg, 10 min) and redispersed in the same amount of aqueous CTAC solution (20 mM). Finally, the nanoparticles are centrifuged once more (20,000 xg, 10 min) and redispersed in water.

*Synthesis of Au@Ag core@shell nanoparticles*. Au@Ag core@shell nanoparticles are synthesized by adapting a previous report.<sup>45</sup> In order to slow down the reaction, the precursor concentrations are modified and a phosphine complexing agent, BSPP is added. In a typical synthesis, an aliquot of Au nanoparticles is added to a CTAC solution (2.7 mL, 66.67 mM) and mixed thoroughly. BSPP solution (90 μL, 375 mM) is then added into it and mixed well. After 10 minutes, AgNO<sub>3</sub> solution (90 μL, 150 mM) and ascorbic acid solution (270 μL, 1500 mM) are added sequentially and mixed well between each addition. The final mixture has an optical density of 2 at the plasmon resonance  $\lambda_{\text{LSPR}} = 540$  nm. The reaction does not occur in the absence of heating or laser irradiation.

*Synthesis under conventional heating in the dark*: 3 mL of the above mixture is transferred to a quartz cuvette (path length of 10 × 10 mm) along with a magnetic stir bar, and sealed. The

cuvette is then placed in a temperature controlled cuvette holder (Qpod 2e/MPKIT) and heated to temperatures ranging from 20 °C to 60 °C, under stirring. Simultaneous extinction spectroscopy is performed by placing a white light source (Energetiq EQ-99XFC LDLS) and a spectrometer (Ocean optics HR 4000), on either sides of the cuvette holder. Multiple neutral density filters are placed to reduce the intensity of the light source (few  $\mu\text{W}/\text{cm}^2$  at 532 nm) passing through the nanoparticle solution.

*Synthesis under laser irradiation at room temperature:* 90  $\mu\text{L}$  of the above solution are transferred to a 10  $\times$  2 mm quartz cuvette, using a micro-syringe. The cuvette is placed in a Thorlabs holder (CVH 100), and is irradiated with a 532 nm laser beam (CNI laser, MGL-FN-532) through one of the 2 mm wide cuvette window. The laser beam has a Gaussian profile with a diameter of 1.5 mm at its  $1/e^2$  power, and the optical power can increase up to 440 mW (corresponding to 25  $\text{W}/\text{cm}^2$ ). Simultaneous extinction spectroscopy is performed by placing a white light source (Energetiq EQ-99XFC LDLS) and a spectrometer (Ocean optics HR 4000), normal to the laser irradiation. Multiple neutral density filters are placed to reduce the intensity of the white light source passing through the nanoparticle solution. A 365 nm long pass filter is also used to filter off any UV light that could induce Ag nucleation. A 532 nm notch filter (Semrock, NF01-532U-25) with a bandwidth of 17 nm, is placed in front of the spectrometer in order to filter any scattered laser light.

*Characterization techniques.* The optical density of the Au nanoparticle suspension is obtained from extinction measurements performed in a Perkin Elmer Lambda 1050 UV-Vis-NIR spectrophotometer, using the Beer-Lambert's relation. Scanning electron microscopy images are

obtained using a Zeiss Sigma field emission SEM operating at 10 kV. HAADF-STEM images and EDX maps are measured on an FEI Verios 460 SEM equipped with a scanning transmission electron microscopy (STEM) retractable detector. The temperature in the irradiated solution is measured using a K-type thermocouple (CHAL-005, Omega Engineering Limited) connected to a data logger (OM-EL-USB-TC, Omega Engineering Limited). Temperature measurements of the cuvette surface are performed using a Fluke Ti20 infrared camera.

*Numerical calculations.* Monte Carlo simulations are implemented in MATLAB, and the heat generation matrix  $q(i_x, i_y, i_z)$  is further used as input in COMSOL simulations. The evolution of the velocity field and the temperature field is numerically obtained from the following set of equations:

$$\begin{aligned}\rho \frac{\partial \mathbf{v}}{\partial t} + \rho(\mathbf{v} \cdot \nabla) \mathbf{v} &= -\nabla p + \mathbf{F} + \nabla(\mu \nabla \mathbf{v}) \\ \frac{\partial \rho}{\partial t} + \nabla \cdot (\rho \mathbf{v}) &= 0 \\ \rho C_p \frac{\partial T}{\partial t} + \rho C_p \mathbf{v} \cdot \nabla T &= \nabla(\kappa \nabla T) + q(i_x, i_y, i_z)\end{aligned}$$

Here  $\mathbf{F}$  is the volume force of buoyancy

$$\mathbf{F} = -g\rho(T)\mathbf{e}_z$$

where  $g$  is the gravitational acceleration,  $\rho$  is the density,  $\mathbf{v}$  is the velocity field,  $p$  is the pressure, and  $T$  is the temperature. Furthermore,  $\mu = \mu(T)$  is the dynamic viscosity,  $\kappa = \kappa(T)$  is the thermal conductivity and  $C_p = C_p(T)$  is the heat capacity at constant pressure. Variations of density are taken into account only in terms of temperature variations. The variations in density may cause an expansion of the fluid, but the direct dynamic effects of those expansions

on the pressure field are neglected (weak compressibility approximation). Realistic temperature-dependent properties of water are taken into account. The above equations reduce to just a heat conduction equation inside the quartz walls of the cuvette, where the velocity field  $\mathbf{v} \equiv 0$ . This problem is solved using a finite element method (COMSOL Multiphysics) with a sufficiently fine mesh. The equations are integrated in time using the backward difference formula. No-slip boundary conditions on the inner cuvette walls are imposed on the nanoparticle suspension, except at the upper surface, which is considered as stress-free. All the outer walls of the cuvette including the bottom one are considered to provide a natural convection to the outside world, with an outward heat flux,  $Q = h (T - T_{ambient})$ . Here,  $h$  is the heat transfer coefficient and  $T_{ambient}$  is chosen as 22.5 °C. The heat transfer coefficient for the bottom wall is tuned such that numerical results match with experimental IR camera measurements on the cuvette external surface.

## ASSOCIATED CONTENT

**Supporting Information Available:** Localized plasmonic heating for CTAC-capped Au nanoparticles; Absorption spectra of Au@Ag nanoparticles with varying shell thicknesses; Spectral sensitivity of the extinction cross-section of Au@Ag nanoparticles; Time evolution of the extinction contrast at different reaction temperatures; Temperature dependence of the extinction spectra of CTAC-capped Au nanoparticles; Extinction contrast vs Ag shell thickness; Setup for plasmon-driven synthesis of Au@Ag core@shell nanoparticles; Light sensitivity of thermocouples; IR camera measurements; Radiation profile of Au nanoparticles; Experimental and simulated temperature increase during laser irradiation; Average solution temperature under 400 mW irradiation; Near-field enhancement; Photosensitivity of Ag growth solution; Absence

of induction in irradiated experiments; Effect of the fraction of irradiated volume (PDF). This material is available free of charge *via* the Internet at <http://pubs.acs.org>.

## AUTHOR INFORMATION

### **Corresponding Author**

\*E-mail: a.baldi@diffen.nl

### **Author Contributions**

The manuscript was written through contributions of all authors. All authors have given approval to the final version of the manuscript.

## ACKNOWLEDGMENT

We gratefully acknowledge Matteo Parente, Ruben Hamans, Gayatri Kumari, Jaime Gómez Rivas, Erik Garnett, Sven Askes, and Jenny Kontoleta for insightful discussions. This work is partially funded by grant 14.0389 of the Stichting voor Fundamenteel Onderzoek der Materie (Foundation for Fundamental Research on Matter, FOM), which is financially supported by the Nederlandse Organisatie voor Wetenschappelijk Onderzoek (Netherlands Organisation for Scientific Research, NWO).

## REFERENCES

- (1) Jin, R.; Cao, Y.; Mirkin, C. A.; Kelly, K. L.; Schatz, G. C.; Zheng, J. G. Photoinduced Conversion of Silver Nanospheres to Nanoprisms. *Science* **2001**, *294*, 1901–1903.

- (2) Zhai, Y.; DuChene, J. S.; Wang, Y.-C.; Qiu, J.; Johnston-Peck, A. C.; You, B.; Guo, W.; DiCiaccio, B.; Qian, K.; Zhao, E. W. Ooi, F.; Hu, D.; Su, D.; Stach, E. A.; Zhu, Z.; Wei, W. D. Polyvinylpyrrolidone-Induced Anisotropic Growth of Gold Nanoprisms in Plasmon-Driven Synthesis. *Nat. Mater.* **2016**, *15*, 889–895.
- (3) Xue, C.; Millstone, J. E.; Li, S.; Mirkin, C. A. Plasmon-Driven Synthesis of Triangular Core-Shell Nanoprisms from Gold Seeds. *Angew. Chem. Int. Ed. Engl.* **2007**, *46*, 8436–8439.
- (4) Millstone, J. E.; Hurst, S. J.; Métraux, G. S.; Cutler, J. I.; Mirkin, C. A. Colloidal Gold and Silver Triangular Nanoprisms. *Small* **2009**, *5*, 646–664.
- (5) Langille, M. R.; Personick, M. L.; Mirkin, C. A. Plasmon-Mediated Syntheses of Metallic Nanostructures. *Angew. Chemie - Int. Ed.* **2013**, *52*, 13910–13940.
- (6) Zhang, J.; Li, S.; Wu, J.; Schatz, G. C.; Mirkin, C. A. Plasmon-Mediated Synthesis of Silver Triangular Bipyramids. *Angew. Chemie* **2009**, *121*, 7927–7931.
- (7) Redmond, P. L.; Walter, E. C.; Brus, L. E. Photoinduced Thermal Copper Reduction onto Gold Nanocrystals under Potentiostatic Control. *J. Phys. Chem. B* **2006**, *110*, 25158–25162.
- (8) Brongersma, M. L.; Halas, N. J.; Nordlander, P. Plasmon-Induced Hot Carrier Science and Technology. *Nat. Nanotechnol.* **2015**, *10*, 25–34.
- (9) Xue, C.; Métraux, G. S.; Millstone, J. E.; Mirkin, C. A. Mechanistic Study of Photomediated Triangular Silver Nanoprism Growth. *J. Am. Chem. Soc.* **2008**, *130*, 8337–8344.

- (10) Maillard, M.; Huang, P.; Brus, L. Silver Nanodisk Growth by Surface Plasmon Enhanced Photoreduction of Adsorbed [Ag<sup>+</sup>]. *Nano Lett.* **2003**, *3*, 1611–1615.
- (11) Wu, X.; Redmond, P. L.; Liu, H.; Chen, Y.; Steigerwald, M.; Brus, L. Photovoltage Mechanism for Room Light Conversion of Citrate Stabilized Silver Nanocrystal Seeds to Large Nanoprisms. *J. Am. Chem. Soc.* **2008**, *130*, 9500–9506.
- (12) Redmond, P. L.; Wu, X.; Brus, L. Photovoltage and Photocatalyzed Growth in Citrate-Stabilized Colloidal Silver Nanocrystals. *J. Phys. Chem. C* **2007**, *111*, 8942–8947.
- (13) Linic, S.; Aslam, U.; Boerigter, C.; Morabito, M. Photochemical Transformations on Plasmonic Metal Nanoparticles. *Nat. Mater.* **2015**, *14*, 567–576.
- (14) Baffou, G.; Quidant, R. Nanoplasmonics for Chemistry. *Chem. Soc. Rev.* **2014**, *43*, 3898–3907.
- (15) Govorov, A. O.; Zhang, H.; Gun'ko, Y. K. Theory of Photoinjection of Hot Plasmonic Carriers from Metal Nanostructures into Semiconductors and Surface Molecules. *J. Phys. Chem. C* **2013**, *117*, 16616–16631.
- (16) Manjavacas, A.; Liu, J. G.; Kulkarni, V.; Nordlander, P. Plasmon-Induced Hot Carriers in Metallic Nanoparticles. *ACS Nano* **2014**, *8*, 7630–7638.
- (17) Besteiro, L. V.; Kong, X.-T.; Wang, Z.; Hartland, G.; Govorov, A. O. Understanding Hot-Electron Generation and Plasmon Relaxation in Metal Nanocrystals: Quantum and Classical Mechanisms. *ACS Photonics* **2017**, *4*, 2759–2781.
- (18) Brown, A. M.; Sundararaman, R.; Narang, P.; Goddard, W. A.; Atwater, H. A.

- Nonradiative Plasmon Decay and Hot Carrier Dynamics: Effects of Phonons, Surfaces, and Geometry. *ACS Nano* **2016**, *10*, 957–966.
- (19) Sundararaman, R.; Narang, P.; Jermyn, A. S.; Goddard III, W. A.; Atwater, H. A. Theoretical Predictions for Hot-Carrier Generation from Surface Plasmon Decay. *Nat. Commun.* **2014**, *5*, 5788.
- (20) Narang, P.; Sundararaman, R.; Atwater, H. A. Plasmonic Hot Carrier Dynamics in Solid-State and Chemical Systems for Energy Conversion. *Nanophotonics* **2016**, *5*, 96–111.
- (21) Baffou, G.; Quidant, R.; Garcia de Abajo, F. J. Nanoscale Control of Optical Heating in Complex Plasmonic Systems. *ACS Nano* **2010**, *4*, 709–716.
- (22) Richardson, H. H.; Carlson, M. T.; Tandler, P. J.; Hernandez, P.; Govorov, A. O. Experimental and Theoretical Studies of Light-to-Heat Conversion and Collective Heating Effects in Metal Nanoparticle Solution. *Nano Lett.* **2009**, *9*, 1139–1146.
- (23) Neumann, O.; Urban, A. S.; Day, J.; Lal, S.; Nordlander, P.; Halas, N. J. Solar Vapor Generation Enabled by Nanoparticles. *ACS Nano* **2013**, *7*, 42–49.
- (24) Neumann, O.; Neumann, A. D.; Silva, E.; Ayala-Orozco, C.; Tian, S.; Nordlander, P.; Halas, N. J. Nanoparticle-Mediated, Light-Induced Phase Separations. *Nano Lett.* **2015**, *15*, 7880–7885.
- (25) Tsao, S. H.; Wan, D.; Lai, Y.-S.; Chang, H.-M.; Yu, C.-C.; Lin, K.-T.; Chen, H.-L. White-Light-Induced Collective Heating of Gold Nanocomposite/Bombyx Mori Silk Thin Films with Ultrahigh Broadband Absorbance. *ACS Nano* **2015**, *9*, 12045–12059.

- (26) Yu, Y.; Sundaresan, V.; Willets, K. A. Hot Carriers *versus* Thermal Effects: Resolving the Enhancement Mechanisms for Plasmon-Mediated Photoelectrochemical Reactions. *J. Phys. Chem. C* **2018**, *122*, 5040–5048.
- (27) Hogan, N. J.; Urban, A. S.; Ayala-Orozco, C.; Pimpinelli, A.; Nordlander, P.; Halas, N. J. Nanoparticles Heat through Light Localization. *Nano Lett.* **2014**, *14*, 4640–4645.
- (28) Baffou, G.; Bon, P.; Savatier, J.; Polleux, J.; Zhu, M.; Merlin, M.; Rigneault, H.; Monneret, S. Thermal Imaging of Nanostructures by Quantitative Optical Phase Analysis. *ACS Nano* **2012**, *6*, 2452–2458.
- (29) Govorov, A. O.; Zhang, W.; Skeini, T.; Richardson, H.; Lee, J.; Kotov, N. A. Gold Nanoparticle Ensembles as Heaters and Actuators: Melting and Collective Plasmon Resonances. *Nanoscale Res. Lett.* **2006**, *1*, 84–90.
- (30) Niu, W.; Zheng, S.; Wang, D.; Liu, X.; Li, H.; Han, S.; Chen, J.; Tang, Z.; Xu, G. Selective Synthesis of Single-Crystalline Rhombic Dodecahedral, Octahedral, and Cubic Gold Nanocrystals. *J. Am. Chem. Soc.* **2009**, *131*, 697–703.
- (31) Zhang, J.; Langille, M. R.; Mirkin, C. A. Photomediated Synthesis of Silver Triangular Bipyramids and Prisms: The Effect of PH and BSPP. *J. Am. Chem. Soc.* **2010**, *132*, 12502–12510.
- (32) Johnson, P. B.; Christy, R. W. Optical Constants of the Noble Metals. *Phys. Rev. B* **1972**, *6*, 4370–4379.
- (33) Muetterties, E. L.; Alegranti, C. W. Solution Structure of Coinage Metal-Phosphine Complexes. *J. Am. Chem. Soc.* **1970**, *92*, 4114–4115.

- (34) Nakano, M.; Fujiwara, T.; Koga, N. Thermal Decomposition of Silver Acetate: Physico-Geometrical Kinetic Features and Formation of Silver Nanoparticles. *J. Phys. Chem. C* **2016**, *120*, 8841–8854.
- (35) Robotjazi, H.; Zhao, H.; Swearer, D. F.; Hogan, N. J.; Zhou, L.; Alabastri, A.; McClain, M. J.; Nordlander, P.; Halas, N. J. Plasmon-Induced Selective Carbon Dioxide Conversion on Earth-Abundant Aluminum-Cuprous Oxide Antenna-Reactor Nanoparticles. *Nat. Commun.* **2017**, *8*, 27.
- (36) Chandrasekhar, R. *Radiative Transfer*; Dover Publications, Inc.: New York, 1960; pp 1–385.
- (37) Yoo, K. M.; Liu, F.; Alfano, R. R. When Does the Diffusion Approximation Fail to Describe Photon Transport in Random Media? *Phys. Rev. Lett.* **1990**, *65*, 2210–2211.
- (38) Wang, L.; Jacques, S. L.; Zheng, L. MCML—Monte Carlo Modeling of Light Transport in Multi-Layered Tissues. *Comput. Methods Programs Biomed.* **1995**, *47*, 131–146.
- (39) Mie, G. Beiträge Zur Optik Trüber Medien, Speziell Kolloidaler Metallösungen. *Ann. Phys.* **1908**, *330*, 377–445.
- (40) Weiss, G. H. Statistical Properties of the Penetration of Photons into a Semi-Infinite Turbid Medium: A Random-Walk Analysis. *Appl. Opt.* **1998**, *37*, 3558–3563.
- (41) Baffou, G.; Quidant, R. Thermo-Plasmonics: Using Metallic Nanostructures as Nano-Sources of Heat. *Laser Photonics Rev.* **2013**, *7*, 171–187.
- (42) Ma, Z.-C.; Chen, Q.-D.; Han, B.; Liu, X.-Q.; Song, J.-F.; Sun, H.-B. Measurement of

Two-Photon Absorption Cross Section of Metal Ions by a Mass Sedimentation Approach. *Sci. Rep.* **2015**, *5*, 17712.

- (43) Liu, Y.; Sonek, G. J.; Berns, M. W.; Konig, K.; Tromberg, B. J. Two-Photon Fluorescence Excitation in Continuous-Wave Infrared Optical Tweezers. *Opt. Lett.* **1995**, *20*, 2246–2248.
- (44) Ueno, K.; Juodkazis, S.; Shibuya, T.; Yokota, Y.; Mizeikis, V.; Sasaki, K.; Misawa, H. Nanoparticle Plasmon-Assisted Two-Photon Polymerization Induced by Incoherent Excitation Source. *J. Am. Chem. Soc.* **2008**, *130*, 6928–6929.
- (45) Ma, Y.; Li, W.; Cho, E. C.; Li, Z.; Yu, T.; Zeng, J.; Xie, Z.; Xia, Y. Au@Ag Core–Shell Nanocubes with Finely Tuned and Well-Controlled Sizes, Shell Thicknesses, and Optical Properties. *ACS Nano* **2010**, *4*, 6725–6734.